

## Active control of electromagnetic fields in layered media

Chaoxian Qi, Shubin Zeng, Neil Jerome A. Egarguin, Daniel Onofrei & Jiefu Chen

To cite this article: Chaoxian Qi, Shubin Zeng, Neil Jerome A. Egarguin, Daniel Onofrei & Jiefu Chen (2024) Active control of electromagnetic fields in layered media, Journal of Electromagnetic Waves and Applications, 38:1, 66-88, DOI: [10.1080/09205071.2023.2270602](https://doi.org/10.1080/09205071.2023.2270602)

To link to this article: <https://doi.org/10.1080/09205071.2023.2270602>



Published online: 29 Nov 2023.



Submit your article to this journal [↗](#)



Article views: 93



View related articles [↗](#)



View Crossmark data [↗](#)



## Active control of electromagnetic fields in layered media

Chaoxian Qi<sup>a</sup>, Shubin Zeng<sup>b</sup>, Neil Jerome A. Egarguin<sup>c</sup>, Daniel Onofrei<sup>d</sup> and Jiefu Chen<sup>a</sup>

<sup>a</sup>Department of Electrical and Computer Engineering, University of Houston, Houston, TX, USA; <sup>b</sup>CGG, Houston, TX, USA; <sup>c</sup>Institute of Mathematical Sciences and Physics, University of the Philippines Los Baños, Los Baños, Laguna, Philippines; <sup>d</sup>Department of Mathematics, University of Houston, Houston, TX, USA

### ABSTRACT

This article presents a numerical strategy for actively manipulating electromagnetic (EM) fields in layered media. In particular, we develop a scheme to characterize an EM source that will generate some predetermined field patterns in prescribed disjoint exterior regions in layered media. The proposed question of specifying such an EM source is not an inverse source problem (ISP) since the existence of a solution is not guaranteed. Moreover, our problem allows for the possibility of prescribing different EM fields in mutually disjoint exterior regions. This question involves a linear inverse problem that requires solving a severely ill-posed optimization problem (i.e. suffering from possible non-existence or non-uniqueness of a solution). The forward operator is defined by expressing the EM fields as a function of the current at the source using the layered media Green's function (LMGF), accounting for the physical parameters of the layered media. This results to integral equations that are then discretized using the method of moments (MoM), yielding an ill-posed system of linear equations. Unlike in ISPs, stability with respect to data is not an issue here since no data is measured. Rather, stability with respect to input current approximation is important. To get such stable solutions, we applied two regularization methods, namely, the truncated singular value decomposition (TSVD) method and the Tikhonov regularization method with the Morozov Discrepancy Principle. We performed several numerical simulations to support the theoretical framework and analyzes, and to demonstrate the accuracy and feasibility of the proposed numerical algorithms.

### ARTICLE HISTORY

Received 1 October 2022  
Accepted 20 August 2023

### KEYWORDS

Antenna radiation pattern synthesis; electromagnetic propagation in nonhomogeneous media; integral equations; Green function; inverse problems; optimization methods

## 1. Introduction

The active manipulation of electromagnetic (EM) fields tackles the problem of characterizing a current (electric and/or magnetic) on the source so that its radiated field approximates desired patterns in prescribed disjoint exterior regions of space. This problem is not an inverse source problem (ISP) since the existence of such an EM source is not guaranteed. In ISPs, the data come from measurements in an exterior region and are associated with a real physical source. This is not the case for our problem as different fields are prescribed on multiple exterior regions. In fact, due to the analyticity of the EM fields, an exact solution

**CONTACT** Jiefu Chen  [jchen84@uh.edu](mailto:jchen84@uh.edu)

may not exist if the field patterns to be realized in the disjoint exterior regions are not all restrictions of the same solution of the exterior Maxwell system. In terms of solutions, stability with respect to data is not an issue in the active EM manipulation problem as no data is measured. The primal concern here is the stability with respect to the approximation of the computed input currents. Moreover, it differs from solving forward EM radiation problems as there is no unique solution (current source) for the proposed control problem due to the existence of non-radiating currents [1,2]. Therefore, the active EM field control problem is treated and solved as an ill-posed optimization problem where we search for a source that will radiate a field that approximates, as well as desired, the prescribed fields in the specified exterior regions. In a way, we study the limits of analytic continuation and one will actually observe numerically, that our proposed strategy is challenged when the control regions with different prescribed EM fields are very close to each other (leading to an unsustainable gradient of the fields).

The study of EM field manipulation has attracted huge attention and research efforts in recent years due to its far-reaching applications. These applications include, but are not limited to, scattering cancelation or reduction (also known as cloaking) [3–11], antenna diagnostics [12–17], partial data near field and intermediate field synthesis or pattern shaping (see [18–27]).

Active EM field control techniques are becoming increasingly ubiquitous to enhance EM wave-based systems. Take the scattering cancelation as an example. The scattering from certain objects, such as combat aircraft, often needs to be reduced to make them invisible to radar, i.e. to reduce the objects' radar cross-section (RCS). An advanced approach for scattering cancelation is active cloaking. The active cloaking scheme seeks to suppress the dominant scattering from the object using an external source. In [4], Chen et al. demonstrated active scattering-cancelation in both 1-D and 3-D scenarios. The authors focused on ensuring broadband invisibility based on anomalous permittivity dispersion. Theoretically, the proposed active cloak scheme can overcome the Bode–Fano bandwidth limit and operate in a much broader bandwidth than passive cloaks. In [5] (see also [6]), the authors explored active EM cloaks using the equivalence principle. External electric and/or magnetic currents are introduced to cancel out the objects' scattered fields subject to a plane wave incidence. More recently, Qian et al. [7] proposed an intelligent cloaking driven by deep learning techniques. The pre-trained deep neural network enables a fast response to an ever-changing incident wave and the surrounding environment without human intervention. This approach allows a wide range of real-time applications, such as moving stealth targets creation schemes and RCS control. In the latter, our strategy can be applied to find suitable feed inputs so that the source cancels the scattering field from a structure in given regions.

Active field control techniques are also prevalent in the area of antenna diagnostics. Lopéz et al. [12] proposed a source reconstruction method (SRM) to establish the equivalent current distribution that radiates the same field as the actual current induced in the antenna under test (AUT). The knowledge of the equivalent currents allows the determination of the antenna radiating elements and the prediction of the AUT-radiated fields outside the equivalent currents domain. In [13], the authors formulated the source reconstruction problem on arbitrary 3-D surfaces using a dual integral equation formulation. The simulations indicate an improved accuracy of the reconstructed current. In [16], Persson et al. applied the equivalent currents approach for radome diagnostics. This work reconstructs

tangential EM fields from a measured far field outside the radome surface. The measured far field is known to be related to the equivalent surface currents on the radome surface using an integral representation. The proposed approach, which includes the mathematical manipulation of integral equations, allows one to locate defect areas on the radome from the far-field data alone.

Active field control can also be helpful in metamaterial or metasurface design. In [28], Brown et al. explored the possibility of metasurface design using the electromagnetic inverse source framework. The electric and magnetic surface susceptibility profiles are computed such that the transmitted field exhibits some desired field specifications. It has been shown that the metasurface can focus the beam from plane waves, change the direction and radiation pattern, etc. Huang et al. [29] reported a reconfigurable metasurface for multifunctional control of EM waves. Recent advances in the study of the hyperbolic metamaterials, such as [30–32] also excited the search for active control strategies for these media, such as those proposed in [33–36].

The research into new active field manipulation methods can play an important role in field synthesis applications. A particular example is field-shaping or field-focusing, which allows efficient wireless power transfer. In [20], Ayestarán et al. used artificial neural networks to realize near-field multi-focusing. It has the advantage of fast prediction of feeding amplitude and phase on each antenna array element. This array synthesis technique can be applied to wireless power transfer. Wireless links between the antenna array and devices are established more efficiently since power radiated at undesired positions or directions can be suppressed. Furthermore, Ayestarán et al. [22] introduced another array synthesis technique that can focus the near field on one or more spots and simultaneously satisfy the far-field specifications. Wu et al. [25] investigated the manipulation of the EM wavefront to realize the near-field power pattern control. Here, the distributions of near-field intensities are given, and source magnitudes are predefined. The algorithm will then find the necessary source phases, which can then be fed to the active antenna array.

To the best of our knowledge, all existing research works regarding the active EM field control assumes that the surrounding medium is homogeneous or free space. Also, most works in EM control are focused on far-field control. Our work is the first one that considers the near-field active EM field control in layered media. Having modern practical applications, such as wireless communication between seawater and air via EM waves, wireless power transfer in subsurface formation, etc., active EM control in layered media is a vital research problem. This article presents a unified framework and a computational platform for active EM manipulation in layered media. Our analysis starts by defining the forward operator that predicts the radiated EM field given the current on the active source using integral equations. Here, the layered media Green's function (LMGF) is employed in the integral equations to account for the physical characteristics of the layered media. Then, we assume an arbitrary 3D closed surface as the EM source, and discretize it using the Rao-Wilton-Glisson (RWG) basis. Accordingly, the continuous integral equations are discretized following the method of moments (MoM), yielding a system of linear equations. This overdetermined linear system is solved in such a way that high accuracy is achieved while requiring less power on the source in the sense of the  $L^2$ -norm (minimum energy) [37–45]. As the system of equations is born out of an inverse problem, it is highly ill-posed. To get a stable solution, we use two regularization methods, namely, the truncated singular value decomposition (TSVD) method and the Tikhonov regularization method with the

Morozov Discrepancy Principle. We perform several simulations to illustrate the feasibility and accuracy of the proposed algorithm.

The rest of this article is organized as follows. Section 2 generally describes the problem and provides relevant theoretical results. Section 3 formulate the integral equation-based forward modeling. We discuss the LMGF and illustrate the MoM. In Section 4, the inversion formulation is presented. Two regularization approaches are introduced, TSVD and the Tikhonov regularization with the Morozov discrepancy principle. Section 5 shows the numerical results of the benchmark examples. Finally, we conclude the article with some remarks in Section 6.

## 2. Theory and formulation

This section presents a general description of the active EM field manipulation problem in layered media and our proposed solution scheme. We cast the active EM field manipulation problem as an inverse problem. The goal is to find an unknown *cause* from its known *effect* [28]. The unified framework of the inverse source problem has already been discussed in [38,39,41,45]. Though some of these works addressed the problem of controlling Helmholtz fields, their approach can be extended to solve EM problems governed by Maxwell’s equations. This article investigates the possibility of controlling the EM fields in layered media. Instead of homogenizing the medium, i.e. replacing an inhomogeneous medium with a homogeneous material with effective parameters [46], we model it as is. This is important especially when one cannot apply multi-scale procedures to homogenize the medium. In the entirety of this work, we assume that the layered medium is horizontally layered, and each layer is composed of a homogeneous material with isotropic or uniaxial (i.e. transverse isotropic) permittivity or permeability. Figure 1 shows the simplified problem geometry. Here, we consider a single source  $D_s$  and two control regions  $D_1$  and  $D_2$ .

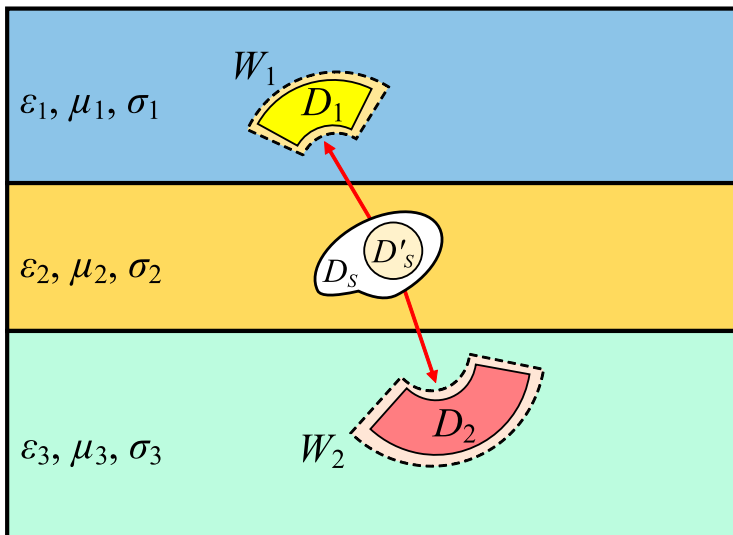


**Figure 1.** Problem geometry showing the control regions  $D_1, D_2$  and the source region  $D_s$  in a layered medium.

$D_1, D_2$  embedded in the layered medium. The number of source and control regions can be arbitrary as shown in the theoretical analysis provided in [38,40,41,45]. The control regions  $D_1$  and  $D_2$  are mutually disjoint domains, i.e.  $D_1 \cap D_2 = \emptyset$ . We also assume that the control regions are well-separated from the source region, i.e.  $(D_1 \cup D_2) \cap D_s = \emptyset$ . In principle, the physical source  $D_s$  can be any arbitrary 3D closed surface. We use a “fictitious source”  $D'_s$ , chosen to be a sphere, compactly embedded in  $D_s$  to rid us of the complications that may be brought about by the possibly complicated shape of the physical EM source. Meanwhile, we slightly enlarge the control regions to the open sets  $W_1$  and  $W_2$  such that  $D_1 \Subset W_1, D_2 \Subset W_2, W_1 \cap W_2 = \emptyset$  and  $(W_1 \cup W_2) \cap D_s = \emptyset$ . As proven in [41] using regularity and uniqueness theorems for the solution of the interior Helmholtz equation, accurate controls on the surfaces  $\partial W_1$  and  $\partial W_2$  ensure smooth controls on  $D_1$  and  $D_2$ . This effectively reduced the dimension of the control problem, from a volumetric control on the entirety of  $D_1$  and  $D_2$  down to a surface control problem on  $\partial W_1$  and  $\partial W_2$ .

In a source-free layered medium in  $\mathbb{R}^3$ , the governing law for EM field radiation are Maxwell's equations

$$\begin{cases} \nabla \times \mathbf{E} &= -j\omega\mu_0\boldsymbol{\mu}\mathbf{H} \\ \nabla \times \mathbf{H} &= j\omega\varepsilon_0\boldsymbol{\varepsilon}\mathbf{E} \end{cases}, \quad (1)$$

where  $\boldsymbol{\varepsilon}$  and  $\boldsymbol{\mu}$  are the complex relative permittivity and relative permeability of the planar stratified media,  $\boldsymbol{\varepsilon} = \mathcal{I}_t\varepsilon_t + \hat{\mathbf{z}}\hat{\mathbf{z}}\varepsilon_z$  and  $\boldsymbol{\mu} = \mathcal{I}_t\mu_t + \hat{\mathbf{z}}\hat{\mathbf{z}}\mu_z$ .  $\mathcal{I}_t$  is the transverse identity dyad. Note that (1) is a general formulation of Maxwell's equations in layered media. If we only consider an isotropic media, the tensors  $\boldsymbol{\varepsilon}$  and  $\boldsymbol{\mu}$  are reduced to scalars. All throughout this paper, the time-harmonic term  $e^{j\omega t}$  is assumed but suppressed.

In this study, our concern is to characterize a boundary input on the EM source so that the EM field it radiates, i.e. the solution to (1), approximates some predetermined fields on the control regions. Mathematically, the problem is to find the boundary input on the source, either a surface electric current  $\mathbf{J} \in \partial D_s$  or a magnetic current  $\mathbf{M} \in \partial D_s$  such that the solutions  $(\mathbf{E}, \mathbf{H})$  of

$$\begin{cases} \nabla \times \mathbf{E} = -j\omega\mu_0\boldsymbol{\mu}\mathbf{H} \text{ and } \nabla \times \mathbf{H} = j\omega\varepsilon_0\boldsymbol{\varepsilon}\mathbf{E} & \text{in } \mathbb{R}^3 \setminus D_s \\ \mathbf{E} \times \hat{\mathbf{n}} = \mathbf{M}, \text{ (or } \hat{\mathbf{n}} \times \mathbf{H} = \mathbf{J}) & \text{on } \partial D_s \\ \text{Silver - M\"uller radiation condition at infinity} & \end{cases} \quad (2)$$

satisfy the control constraints

$$\begin{cases} \|\mathbf{E} - \mathbf{E}_j\|_{C(D_j)} \leq \delta & \text{for } j = \overline{1, 2} \\ \|\mathbf{H} - \mathbf{H}_j\|_{C(D_j)} \leq \delta & \text{for } j = \overline{1, 2} \end{cases}, \quad (3)$$

where  $\delta$  is the desired control accuracy threshold. In (2),  $\hat{\mathbf{n}}$  is the unit exterior normal vector to  $\partial D_s$ . The Silver-M\"uller radiation condition in (2) at infinity is defined following [47] as

$$\begin{cases} \mathbf{E}(\mathbf{x}) \times \hat{\mathbf{x}} + \frac{1}{Y}\mathbf{H}(\mathbf{x}) = \mathcal{O}(1/|\mathbf{x}|^2) \\ \mathbf{H}(\mathbf{x}) \times \hat{\mathbf{x}} - Y\mathbf{E}(\mathbf{x}) = \mathcal{O}(1/|\mathbf{x}|^2) \end{cases} \quad (4)$$

as  $|\mathbf{x}| \rightarrow \infty$  uniformly with respect to  $\hat{\mathbf{x}} \in \partial D_s$ . The vector  $\hat{\mathbf{x}} = \frac{\mathbf{x}}{|\mathbf{x}|}$  represents the unit vector pointing in the same direction as  $\mathbf{x}$ , while  $Y = \sqrt{\frac{\varepsilon}{\mu}}$  is the admittance in non-conductive

media. The radiation conditions force that every solution  $(\mathbf{E}, \mathbf{H})$  must decay as fast as how  $\frac{1}{|\mathbf{x}|}$  does as  $\mathbf{x} \rightarrow \infty$ .

**Remark 2.1:** In [38], the authors proposed an active control strategy for acoustic fields in a two-layered ocean strategy. That can be extended to the EM paradigm through the formalism developed in [45] that employed Debye potentials. Some preliminary numerical tests were presented in [48]. Other related works on EM control using Debye potentials can be found in [49–53].

### 3. Integral equation representation

To obtain the Green's function in layered media, we need to transform the time-harmonic Maxwell's equations from the spatial domain into the spectral domain by taking the 2D Fourier transform. Physically speaking, the Fourier transformation converts a dipole source in a spatial domain into an infinite series of plane waves in the spectral domain. The modeling of plane waves propagating in layered media can be solved using the transmission line analogy [54]. First, we define the Fourier transform pair,

$$\tilde{\mathcal{F}}(\mathbf{k}_\rho) = \int_{-\infty}^{\infty} \int_{-\infty}^{\infty} \mathcal{F}(\boldsymbol{\rho}) e^{j\mathbf{k}_\rho \cdot \boldsymbol{\rho}} dx dy \quad (5)$$

and

$$\mathcal{F}(\boldsymbol{\rho}) = \frac{1}{(2\pi)^2} \int_{-\infty}^{\infty} \int_{-\infty}^{\infty} \tilde{\mathcal{F}}(\mathbf{k}_\rho) e^{-j\mathbf{k}_\rho \cdot \boldsymbol{\rho}} dk_x dk_y, \quad (6)$$

where  $\mathcal{F}$  can be a scalar, vector, or dyadic quantity. Here,  $\boldsymbol{\rho} = x\hat{\mathbf{x}} + y\hat{\mathbf{y}}$  is the transverse component of the position vector  $\mathbf{r}$ , i.e.  $\mathbf{r} = \boldsymbol{\rho} + z\hat{\mathbf{z}}$ , while  $\mathbf{k}_\rho = k_x\hat{\mathbf{x}} + k_y\hat{\mathbf{y}}$  is the transverse component of the wavenumber. Applying (5) to (1), we obtain the spectral-domain form of Maxwell's equations,

$$\begin{cases} \tilde{\nabla} \times \tilde{\mathbf{E}} = -j\omega\mu_0\boldsymbol{\mu}\tilde{\mathbf{H}} \\ \tilde{\nabla} \times \tilde{\mathbf{H}} = j\omega\varepsilon_0\boldsymbol{\varepsilon}\tilde{\mathbf{E}} \end{cases} \quad (7)$$

From the transmission line analogy, the transformed fields can now be written directly in terms of transformed dyadic Green's functions as:

$$\begin{aligned} \tilde{\mathbf{E}}(\mathbf{k}_\rho, z) = & \int_{-\infty}^{\infty} \left[ \tilde{\mathcal{G}}^{EJ}(\mathbf{k}_\rho, z, z') \cdot \tilde{\mathbf{J}}(\mathbf{k}_\rho, z') \right. \\ & \left. + \tilde{\mathcal{G}}^{EM}(\mathbf{k}_\rho, z, z') \cdot \tilde{\mathbf{M}}(\mathbf{k}_\rho, z') \right] dz', \end{aligned} \quad (8)$$

and

$$\begin{aligned} \tilde{\mathbf{H}}(\mathbf{k}_\rho, z) = & \int_{-\infty}^{\infty} \left[ \tilde{\mathcal{G}}^{HJ}(\mathbf{k}_\rho, z, z') \cdot \tilde{\mathbf{J}}(\mathbf{k}_\rho, z') \right. \\ & \left. + \tilde{\mathcal{G}}^{HM}(\mathbf{k}_\rho, z, z') \cdot \tilde{\mathbf{M}}(\mathbf{k}_\rho, z') \right] dz', \end{aligned} \quad (9)$$

where the functions,  $\tilde{\mathcal{G}}^{EJ}$ ,  $\tilde{\mathcal{G}}^{EM}$ ,  $\tilde{\mathcal{G}}^{HJ}$ , and  $\tilde{\mathcal{G}}^{HM}$  in the square brackets on the right-hand side in (8) and (9) can be expressed using the transmission line analogy of voltages and currents. More detailed expressions of dyadic Green's functions in the spectral domain are given in [54]. As long as we obtain the Green's function in the spectral domain, we are ready to calculate their spatial-domain forms using (6). For instance, let's consider the electric field. Taking the inverse Fourier transform of (8), we can write the electric field in the spatial domain as

$$\begin{aligned} \mathbf{E}(\mathbf{r}) = & \int_{-\infty}^{\infty} \int_{-\infty}^{\infty} \int_{-\infty}^{\infty} [\mathcal{G}^{EJ}(\boldsymbol{\rho} - \boldsymbol{\rho}', z, z') \cdot \mathbf{J}(\mathbf{r}') \\ & + \mathcal{G}^{EM}(\boldsymbol{\rho} - \boldsymbol{\rho}', z, z') \cdot \mathbf{M}(\mathbf{r}')] dx' dy' dz', \end{aligned} \quad (10)$$

where  $\mathcal{G}^{EJ}$  is a dyadic tensor and it can be evaluated through the integral

$$\begin{aligned} \mathcal{G}^{EJ}(\boldsymbol{\rho} - \boldsymbol{\rho}', z, z') \\ = \frac{1}{(2\pi)^2} \int_{-\infty}^{\infty} \int_{-\infty}^{\infty} \tilde{\mathcal{G}}^{EJ}(\mathbf{k}_\rho, z, z') e^{-j\mathbf{k}_\rho \cdot (\boldsymbol{\rho} - \boldsymbol{\rho}')} dk_x dk_y. \end{aligned} \quad (11)$$

Note that the function  $\mathcal{G}^{EM}$  in (10), and consequently the magnetic field, can be evaluated in a similar procedure. To accelerate the numerical calculation of the integrals in (11) and its analogs for the magnetic field, we use the Hankel transform. This transformation reduces the double into a single integral known as a Sommerfeld-type (or simply Sommerfeld) integral (SI). More details can be found in Appendix. With a rigorous manipulations and derivations, all the components of dyadic Green's function in layered media involving general electric and magnetic sources can be expressed in terms of 16 independent SIs [55]. These expressions are shown in Appendix.

The evaluation of the SIs in (A1) is usually carried out in the numerically. Various algorithms were developed for the accurate and efficient evaluation of these independent SIs, including the deformed integral path method [56], asymptotic singularity extraction [55,57,58], and the weighted average method for integral tails [59,60].

For simplicity, we can express the integrals for evaluating  $\mathbf{E}$  and  $\mathbf{H}$  in the compact form

$$\begin{aligned} \begin{bmatrix} \mathbf{E}(\mathbf{r}) \\ \mathbf{H}(\mathbf{r}) \end{bmatrix} = & \mathcal{K}\{\mathbf{J}(\mathbf{r}'), \mathbf{M}(\mathbf{r}')\} \\ = & \left[ \langle \mathcal{G}^{EJ}(\mathbf{r}, \mathbf{r}'); \mathbf{J}(\mathbf{r}') \rangle + \langle \mathcal{G}^{EM}(\mathbf{r}, \mathbf{r}'); \mathbf{M}(\mathbf{r}') \rangle \right] \\ & + \left[ \langle \mathcal{G}^{HJ}(\mathbf{r}, \mathbf{r}'); \mathbf{J}(\mathbf{r}') \rangle + \langle \mathcal{G}^{HM}(\mathbf{r}, \mathbf{r}'); \mathbf{M}(\mathbf{r}') \rangle \right], \end{aligned} \quad (12)$$

where the notation  $\langle ; \rangle$  denotes the integral of product of the two functions separated by the semicolon over their common spatial support. To evaluate the integrals numerically, MoM is applied to reduce the continuous integrals to discrete EM moments. This is realized by discretizing the source surface  $\partial D_s$  into finite triangle patches such that the surface currents can be expressed as

$$\begin{cases} \mathbf{J}(\mathbf{r}') = \sum_{n=1}^N I_n^S \mathbf{\Lambda}_n(\mathbf{r}') \\ \mathbf{M}(\mathbf{r}') = \sum_{n=1}^N V_n^S \mathbf{\Lambda}_n(\mathbf{r}') \quad \mathbf{r}' \in \partial D_s, \end{cases}, \quad (13)$$

where  $N$  is the total number of basis functions. Moreover,  $\mathbf{I}^S = [I_1^S \ I_2^S \ \dots \ I_N^S]$  and  $\mathbf{V}^S = [V_1^S \ V_2^S \ \dots \ V_N^S]$  are two vectors whose elements are the coefficients of discretized surface currents  $\mathbf{J}$  and  $\mathbf{M}$ . Each  $\mathbf{\Lambda}_n$  is a divergence-conforming Rao-Wilton-Glisson (RWG) basis function as defined in [61].

#### 4. Inversion

In Section 3, we used the integral equation method to define the forward operator. Thus, if the electric and magnetic currents are given, the EM fields can be evaluated via the forward operator  $\mathcal{K}$  defined in (12). In contrast to this forward problem of determining the radiation field of a given current source, the electromagnetic inverse source problem aims to find an unknown *cause* from its known *effect* [28]. Following the same strategy in [38,39,41–43,45], the integral equation

$$\mathcal{K}(\mathbf{J}, \mathbf{M}) = (\mathbf{E}, \mathbf{H}) \quad (14)$$

on the control regions is converted into a system of linear equations by discretizing the control regions and source into discrete meshes. This results to the linear system in matrix form

$$\mathbf{A}\mathbf{w}_d = \mathbf{b}, \quad (15)$$

where  $\mathbf{w}_d = [\mathbf{I}^S; \mathbf{V}^S]$  is a vector containing the unknown coefficients in the RWG basis expansion of the sought inputs  $(\mathbf{J}, \mathbf{M})$  given in (13). Meanwhile,  $\mathbf{A}$  represents the matrix of moments computed from the propagator  $\mathcal{K}$ , and  $\mathbf{b}$  is the vector of values of  $(\mathbf{E}, \mathbf{H})$  at the mesh of evaluation points distributed within the control regions. Since we wish to have a large number of evaluation points in the control regions while having as few degrees of freedom as possible, the number of rows of  $\mathbf{A}$  will be much greater than the number of columns. Thus,  $\mathbf{A}$  is not square and consequently,  $\mathbf{w}_d$  can't be computed as  $\mathbf{A}^{-1}\mathbf{b}$ . In fact, the overdetermined system of equations in (15) will have no exact solution. The problem now becomes finding a solution  $\mathbf{w}_d$  that “best” approximates the field represented by  $\mathbf{b}$ . If one is only concerned with the proximity of the generated field values  $\mathbf{A}\mathbf{w}_d$  at the control points to the prescribed values  $\mathbf{b}$ , then the desired solution coincides with the solution of

the optimization problem

$$\hat{\mathbf{w}}_d = \arg \min_{\mathbf{w}_d \in \partial D_s} \left[ \sum_{j=1}^2 \xi_j \|\mathbf{A}_j \mathbf{w}_d - \mathbf{b}_j\|_{L^2(\partial W_j)}^2 \right], \quad (16)$$

where  $\xi_j, j = \overline{1, 2}$  are the weights balancing the residuals on the control regions.

The optimization problem (16) is a classical least-squares inversion of the linear system (15). However, this linear system is ill-posed since it is induced by an inverse problem. Hence, the solution given in (16) will be unstable with respect to perturbations in the right hand side data and/or manufacturing noise. To avoid these instabilities, we seek regularized solutions. To obtain such, we employ two commonly used regularization approaches, namely, the truncated singular value decomposition (TSVD) and the Tikhonov regularization with the Morozov discrepancy principle [62,63]. The TSVD method utilizes only the most dominant singular values of the coefficient matrix  $\mathbf{A}$  rather than the full set as in the usual singular value decomposition. It is often straightforward to implement, though the computational cost is usually high especially for matrices with large dimensions. On the other hand, Tikhonov regularization is typically the method of first choice for most linear problems. It provides an opportunity to impose additional constraints or conditions on the solutions sought [62]. Generally, Tikhonov methods are less computationally expensive than the TSVD. However, bulk of the work revolves on resolving the question ‘‘How to choose the regularization parameter?’’. In the remainder of this section we elaborate on these techniques leading to two algorithms solving the active EM field manipulation problem.

It is known that any matrix  $\mathbf{A} \in \mathbb{R}^{m \times n}$  can be written in the form,

$$\mathbf{A} = \mathbf{U} \mathbf{D} \mathbf{V}^T \quad (17)$$

where the superscript ‘‘T’’ represents the matrix transpose, and  $\mathbf{U} \in \mathbb{R}^{m \times m}$  and  $\mathbf{V} \in \mathbb{R}^{n \times n}$  are orthogonal matrices, i.e.  $\mathbf{U}^T \mathbf{U} = \mathbf{U} \mathbf{U}^T = \mathbf{I}$ , and  $\mathbf{V}^T \mathbf{V} = \mathbf{V} \mathbf{V}^T = \mathbf{I}$  where  $\mathbf{I}$  is the identity matrix. Moreover,  $\mathbf{D} \in \mathbb{R}^{m \times n}$  is a diagonal matrix whose diagonal elements  $d_j$  are the singular values of  $\mathbf{A}$ . The minimum norm solution of the equation  $\mathbf{A} \mathbf{x} = \mathbf{b}$  is given by

$$\mathbf{x} = \mathbf{V} \mathbf{D}^{-} \mathbf{U}^T \mathbf{b}, \quad (18)$$

where  $\mathbf{D}^{-}$  is the diagonal matrix with diagonal elements  $d_j^{-1}$ . Numerical instabilities may occur when the  $r$ th diagonal element  $d_r$  in  $\mathbf{D}$  is much smaller than  $d_1$ , i.e.  $d_r^{-1}$  appearing in  $\mathbf{D}^{-}$  is much larger than  $d_1^{-1}$ . To tackle this bad conditioning, we ignore the diagonal elements that are below a defined threshold. This is the truncated SVD (TSVD) method. Hence, the TSVD solution is given by

$$\hat{\mathbf{w}}_d = \mathbf{V} \mathbf{D}_t^{-} \mathbf{U}^T \mathbf{b}, \quad (19)$$

where  $t$  denotes the number of diagonal elements in the truncated matrix.

The Tikhonov regularization method, on the other hand, requires a regularization parameter as a penalty weight for the power required by the solution. Hence, the corresponding optimization problem

$$\hat{\mathbf{w}}_d = \arg \min_{\mathbf{w}_d \in \partial D_s} \left[ \sum_{j=1}^2 \xi_j \|\mathbf{A}_j \mathbf{w}_d - \mathbf{b}_j\|_{L^2(\partial W_j)}^2 + \alpha \|\mathbf{w}_d\|_{L^2(\partial D'_s)}^2 \right], \quad (20)$$

where  $\alpha > 0$  is the regularization parameter. In this formalism, the Tikhonov solution can be regarded as a balance between two requirements, namely

- (1)  $\hat{\mathbf{w}}_d$  should give a small residual  $\mathbf{A} \mathbf{w}_d - \mathbf{b}$ ; and
- (2)  $\hat{\mathbf{w}}_d$  should be small in the sense of  $L^2$ -norm.

The regularization parameter  $\alpha$  is selected to minimize the misfit while keeping the solution norm small thereby stabilizing it with respect to data noise. The optimal  $\alpha$  is determined by the Morozov's discrepancy principle. See [62,63] for a detailed exposition. Once the optimal  $\alpha$  is determined, the solution of (20) is given by

$$\hat{\mathbf{w}}_d = (\alpha \mathbf{I} + \mathbf{A}^* \mathbf{A})^{-1} \mathbf{A}^* \mathbf{b}, \quad (21)$$

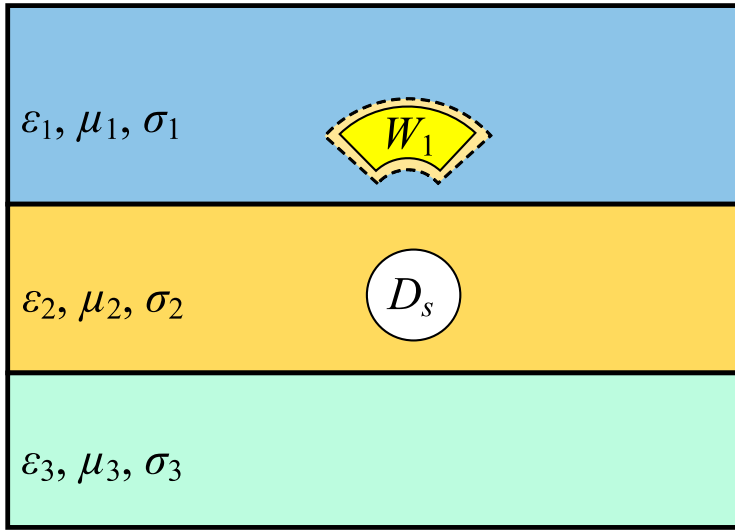
where  $\mathbf{A}^*$  is the complex conjugate transpose of  $\mathbf{A}$ .

These two regularization methods give rise to two different numerical solution schemes for the active EM manipulation problem. These approaches are formalized in Algorithms 1 and 2. In the next section, we provide numerical simulations illustrating these schemes and comparing the solutions obtained from them.

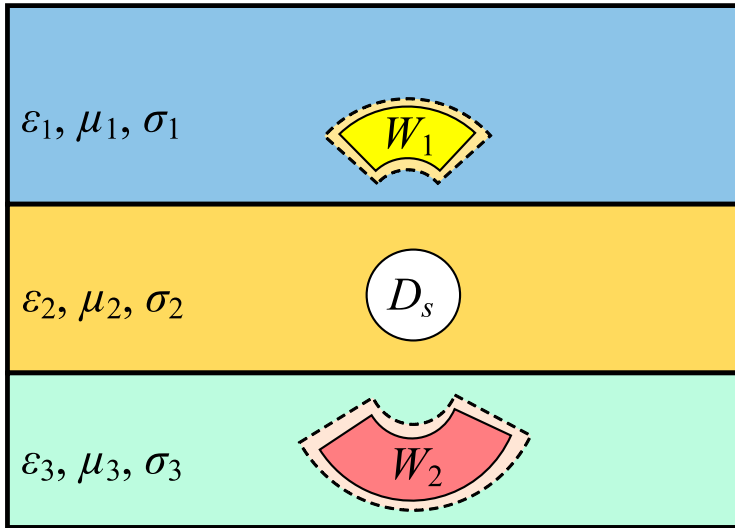
## 5. Numerical results

To illustrate the proposed algorithms and demonstrate their feasibility, we present several numerical simulations. For an illustration purposes, we consider a three-layer medium as shown in Figure 2. First, we investigate the EM field control in one near control region depicted in Figure 2a. Then, we extend our numerical study into a multiple-region regime with two near-field control regions  $W_1$  and  $W_2$  as sketched in Figure 2b. The control regions and the source are placed in different layers. Note that the control regions can be in the same layer as the source. As stated above, our use of a fictitious source  $D'_s \in D_s$  in the formulation allows the physical source  $D_s$  to have an arbitrary shape as long as it has a Lipschitz continuous boundary and is well separated from the control regions.

In all simulations, we apply the the two approaches summarized in Algorithms 1 and 2. The specific runs are labeled the “integral equation- TSVD” and the “integral equation- Tikhonov” methods, respectively. We compare the performance of these two methods based on accuracy and the solution norm. To gauge the accuracy, i.e. the proximity of the generated fields to the prescribed field values on the control points, we use the following measures of error. First, we look at a global measure of error, the  $L^2$  relative error defined



(a)



(b)

**Figure 2.** Problem geometry: control region(s)  $W_1, W_2$ , and the source region  $D_s$  in layered media. (a) One control region. (b) Two control regions.

as

$$\|err\|_{L^2(\partial W_j)} = \begin{cases} \frac{\|\mathbf{G}_j - \mathbf{P}_j\|_{L^2(\partial W_j)}}{\|\mathbf{P}_j\|_{L^2(\partial W_j)}} & \text{if } \|\mathbf{P}_j\|_{L^2(\partial W_j)} \neq 0, \\ \|\mathbf{G}_j - \mathbf{P}_j\|_{L^2(\partial W_j)} & \text{if } \|\mathbf{P}_j\|_{L^2(\partial W_j)} = 0, \end{cases} \quad (22)$$

---

**Algorithm 1:** TSVD Regularization
 

---

**input :** Prescribed fields,  $(\mathbf{E}_j, \mathbf{H}_j)$  in  $D_j, j = \overline{1, 2}$ ,  
 accuracy threshold  $\delta$ .

- 1  $(\mathbf{I}^S, \mathbf{V}^S) \leftarrow (\mathbf{J}, \mathbf{M})$  using (13),
- 2  $\mathbf{b}_j \leftarrow (\mathbf{E}_j, \mathbf{H}_j)$ ,
- 3  $\mathbf{b} = [\mathbf{b}_1; \mathbf{b}_2]$ ,
- 4 **for**  $n = 1$  to  $N$  **do**
- 5     Compute  $\mathcal{G}_n^{EJ}, \mathcal{G}_n^{EM}, \mathcal{G}_n^{HJ}, \mathcal{G}_n^{HM}$  via (A2)–(A5),
- 6 **end**
- 7  $\mathbf{A}_j = \begin{bmatrix} \mathcal{G}_j^{EJ}, \mathcal{G}_j^{EM} \\ \mathcal{G}_j^{HJ}, \mathcal{G}_j^{HM} \end{bmatrix}$ ,
- 8  $\mathbf{A} = [\mathbf{A}_1; \mathbf{A}_2]$ ,
- 9  $\mathbf{A} = \mathbf{U}\mathbf{D}\mathbf{V}^T, \mathbf{D}^- = \text{pinv}(\mathbf{D})$ ,
- 10  $t \leftarrow 1000$ , truncate the first 1000 singular values,
- 11  $\mathbf{w}_d = \mathbf{V}\mathbf{D}_t^- \mathbf{U}^T \mathbf{b}$ ,
- 12  $\tau^2 = \left[ \sum_{j=1}^2 \xi_j \|\mathbf{A}_j \mathbf{w}_d - \mathbf{b}_j\|^2 \right]$ ,
- 13 **while**  $\tau^2 > \delta^2$  **do**
- 14      $t \leftarrow (t + 100)$ ,
- 15      $\mathbf{w}_d = \mathbf{V}\mathbf{D}_t^- \mathbf{U}^T \mathbf{b}$ ,
- 16      $\tau^2 = \left[ \sum_{j=1}^2 \xi_j \|\mathbf{A}_j \mathbf{w}_d - \mathbf{b}_j\|^2 \right]$ .
- 17 **end**
- 18  $(\mathbf{I}^S, \mathbf{V}^S) \leftarrow \mathbf{w}_d$ ,
- 19  $(\mathbf{J}, \mathbf{M}) \leftarrow (\mathbf{I}^S, \mathbf{V}^S)$ ,

**output:** Surface currents  $\mathbf{J}$  and/or  $\mathbf{M} \in D_s$ .

---

for each  $j = \overline{1, 2}$ . Here,  $\mathbf{G}_j = \mathbf{A}_j \mathbf{w}_d$  denotes the generated field while  $\mathbf{P}_j$  is the prescribed field.  $\mathbf{G}_j$  and  $\mathbf{P}_j$  can either be  $\mathbf{E}$  or  $\mathbf{H}$ . This is a quantitative measure of control performance all throughout the control regions. Then we also consider a more local measure of error, the pointwise error given by

$$\text{err}_i = \begin{cases} \frac{|G_i - P_i|}{|P_i|} & \text{if } P_i \neq 0, \\ |G_i - P_i| & \text{if } P_i = 0, \end{cases} \quad (23)$$

where  $\text{err}_i$  is the relative or absolute error in the  $i$ th evaluation point. For the solution norm, we take note of the power radiated by the source in terms of decibels.

### 5.1. One control region

We start from a simple geometry where only one control region and one source are present. The background medium is horizontally layered and transverse isotropic. From top to

**Algorithm 2:** Tikhonov Regularization

---

**input** : Prescribed fields,  $(\mathbf{E}_j, \mathbf{H}_j)$  in  $D_j, j = \overline{1, 2}$ ,  
accuracy threshold  $\delta$ .

- 1  $(\mathbf{I}^S, \mathbf{V}^S) \leftarrow (\mathbf{J}, \mathbf{M})$  using (13),
- 2  $\mathbf{b}_j \leftarrow (\mathbf{E}_j, \mathbf{H}_j)$ ,
- 3  $\mathbf{b} = [\mathbf{b}_1; \mathbf{b}_2]$ ,
- 4 **for**  $n = 1$  **to**  $N$  **do**
- 5 | Compute  $\mathcal{G}_n^{EJ}, \mathcal{G}_n^{EM}, \mathcal{G}_n^{HJ}, \mathcal{G}_n^{HM}$  via (A2)–(A5),
- 6 **end**
- 7  $\mathbf{A}_j \leftarrow \begin{bmatrix} \mathcal{G}_n^{EJ}, \mathcal{G}_n^{EM} \\ \mathcal{G}_n^{HJ}, \mathcal{G}_n^{HM} \end{bmatrix}$ ,
- 8  $\mathbf{A} = [\mathbf{A}_1; \mathbf{A}_2]$ ,
- 9  $\alpha \leftarrow 10^{-12}$ ,
- 10  $\beta \leftarrow 1.05$ ,
- 11  $\mathbf{w}_d = (\alpha \mathbf{I} + \mathbf{A}^* \mathbf{A})^{-1} \mathbf{A}^* \mathbf{b}$ ,
- 12  $\tau^2 = \left[ \sum_{j=1}^2 \xi_j \|\mathbf{A}_j \mathbf{w}_d - \mathbf{b}_j\|^2 + \alpha \|\mathbf{w}_d\|^2 \right]$ ,
- 13 **while**  $\tau^2 > \delta^2$  **do**
- 14 |  $\alpha \leftarrow \frac{\alpha}{\beta}$ ,
- 15 |  $\mathbf{w}_d = (\alpha \mathbf{I} + \mathbf{A}^* \mathbf{A})^{-1} \mathbf{A}^* \mathbf{b}$ ,
- 16 |  $\tau^2 = \left[ \sum_{j=1}^2 \xi_j \|\mathbf{A}_j \mathbf{w}_d - \mathbf{b}_j\|^2 + \alpha \|\mathbf{w}_d\|^2 \right]$ ,
- 17 **end**
- 18  $(\mathbf{I}^S, \mathbf{V}^S) \leftarrow \mathbf{w}_d$ ,
- 19  $(\mathbf{J}, \mathbf{M}) \leftarrow (\mathbf{I}^S, \mathbf{V}^S)$ ,

**output:** Surface currents  $\mathbf{J}$  and/or  $\mathbf{M} \in D_s$ .

---

bottom, the relative permittivity is given by  $\varepsilon_r$  is  $[1, 2, 1]$ . The conductivity is zero, i.e. the medium is lossless. The entire layered medium is also assumed to be non-magnetic, i.e.  $\mu_r = [1, 1, 1]$ . The control region is an annular sector and satisfies  $D_1 \Subset W_1$ , where  $W_1$  is defined in the spherical coordinates (with respect to the origin) by

$$W_1 = \left\{ (r, \theta, \phi) : r \in [0.5, 0.55], \theta \in \left[ -\frac{\pi}{4}, \frac{\pi}{4} \right], \right. \\ \left. \phi \in \left[ \frac{3\pi}{4}, \frac{5\pi}{4} \right] \right\} + [0.3, 0, 0]. \quad (24)$$

It should be noted that the use of spherical coordinates allows a simpler representation of  $W_1$ . But when we calculate the Green's functions involving the observation and source points, we convert the spherical mesh coordinates on the annular sector to Cartesian coordinates. In our experiment, the operating frequency is 47.7 MHz (corresponding to wave number  $k = 1$ ). Throughout this subsection, we use the sphere of radius 0.31 m centered

at the origin as the physical source  $D_s$ . The fictitious source  $D'_s$ , on which all calculations were done, is the sphere of radius 0.30 m centered at the origin. We assume that only electric current  $\mathbf{J}$  is present on  $D_s$ . We use 2808 triangle patches in the RWG decomposition of the unknown current resulting to 4212 degrees of freedom (DoF). The prescribed field in  $W_1$  is a plane wave with electric field

$$\mathbf{E}(x, y, z) = \hat{\mathbf{x}}\mathbf{E}_0 \cdot e^{-jkz}, \quad (25)$$

where  $k = 1$  is the wavenumber in the top layer. The magnetic field can be attained through

$$\mathbf{H}(\mathbf{r}) = \frac{1}{\omega\mu} \hat{\mathbf{z}} \times \mathbf{E}(\mathbf{r}). \quad (26)$$

This EM wave propagates along the  $\hat{\mathbf{z}}$  direction, and the electric field is polarized in the  $\hat{\mathbf{x}}$  direction. We wish to match this EM field on a mesh of points on the surface of the control regions. Here, we consider a mesh with 2750 evaluation points. For each of these points, we match three components of the electric field and another three for the magnetic field. Hence, the coefficient matrix of the linear system has 16,500 rows and 4212 columns. Further increasing the number of mesh points for the control region will make the system too large for numerical calculations and storage.

Figure 3 shows the  $\mathbf{E}$  and  $\mathbf{H}$  obtained by the “integral equation- TSVD” method. Only non-zero components  $\mathbf{E}_x$  and  $\mathbf{H}_y$  are displayed. In Figure 3, the first row shows the results of the  $\mathbf{E}_x$  synthesis, while the second row shows the one for  $\mathbf{H}_y$ . The three columns on each row display the prescribed field, generated field, and pointwise relative error. Note that only the real parts of the fields is shown here since the imaginary part exhibits similar results. One can notice that the generated fields, both electric and magnetic, almost have the same pattern as the prescribed fields. Though some artifacts are observed in the generated fields, the maximum relative error of the approximated fields is less than 0.1. The overall  $L^2$ -norm error is within the order  $10^{-3}$ . Similarly, we perform the experiment using the “integral equation-Tikhonov” method. Figure 4 demonstrates the control performance. We notice the approximated  $\mathbf{E}_x$  is almost the same as that in Figure 3. However, the generated  $\mathbf{H}_y$  in Figure 4 is worse than the “integral equation-TSVD” method. There are points where the pointwise relative error exceeds 0.1.

The characterized currents are shown in Figure 5, where Figure 5(a,b) correspond to the results of the “integral equation-TSVD” method and “integral equation-Tikhonov” method. Due to the wide range of the current magnitude on  $D_s$ , we make use of the logarithmic scale of current density, i.e. dB A m<sup>-2</sup>. We observe that the computed current has an irregular distribution, and its amplitude is considerable in some areas. The characterized current source is a high-power source for both approaches.

From the accuracy perspective, the TSVD regularization is better than the Tikhonov regularization. We observed that the Tikhonov regularized solution is the same as the SVD solution as long as the regularization parameter  $\alpha$  is sufficiently small (smaller than the smallest singular value [62]). With regards to the solution norm, the current obtained by the “integral equation-TSVD” method is about 20 dB larger than the “integral equation-Tikhonov” method. If the power budget is a primal concern, then the current source obtained through the Tikhonov regularization is more desired as it requires a lower power consumption.

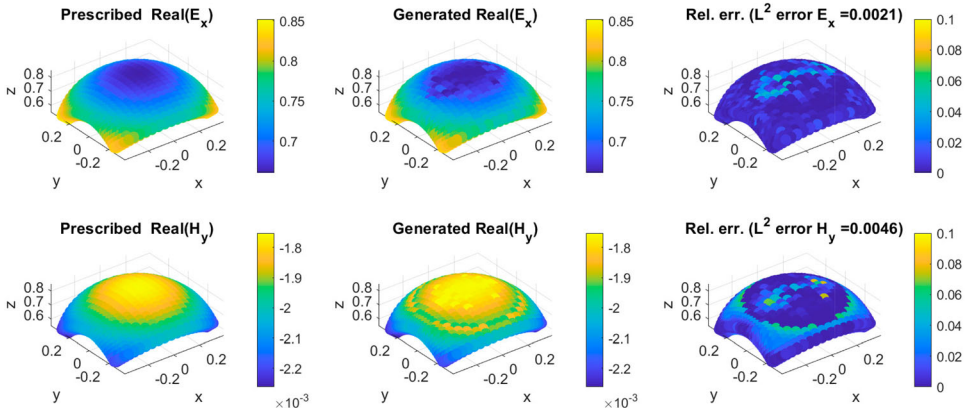


**Figure 3.** Electric and magnetic field synthesis in an exterior control region by “integral equation-TSVD” method.

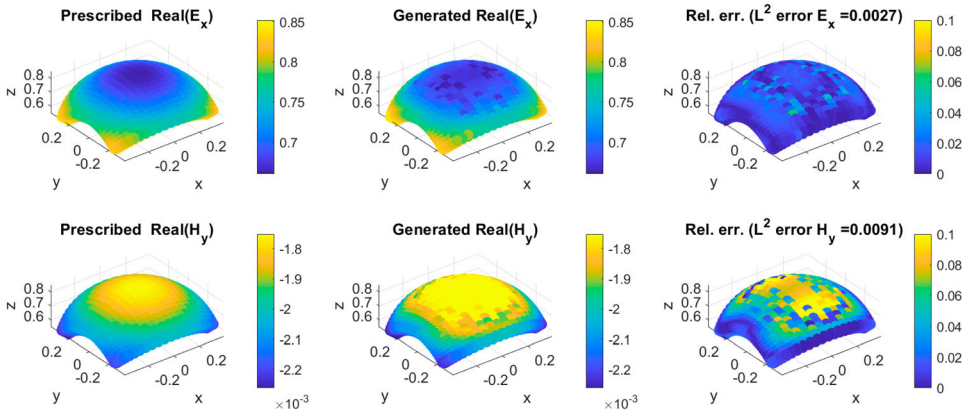


**Figure 4.** Electric and magnetic field synthesis in an exterior control region by “integral equation-Tikhonov” method.

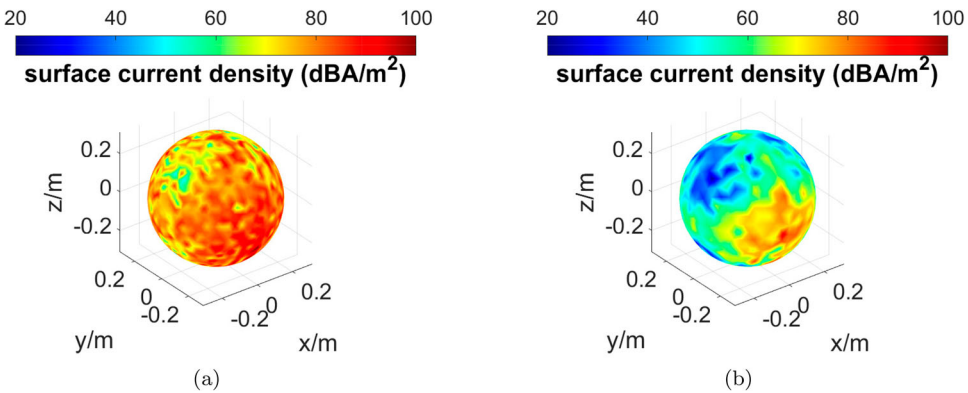


**Figure 5.** Characterized surface electric current ( $\mathbf{J}$ ) on the source  $\partial D_S$ . (a) “integral equation-TSVD” method. (b) “integral equation-Tikhonov” method.

**Remark 5.1:** Note that the Tikhonov approach addresses the minimum energy solution (with  $\|\cdot\|_{L^2}$ ), while the TSVD approach does not. That is why the two solutions appear differently in Figure 5.

## 5.2. Two control regions

In this subsection, we perform active EM field control in two exterior control regions. We examine the performance of our framework in creating a plane EM wave in  $W_1$  and null field in  $W_2$ . This technique could be potentially used for wireless power transfer or EM contrast control, where the EM wave is projected in a target area while the power radiated in undesired regions is suppressed. The problem geometry is shown in Figure 2b, where  $W_1$ ,  $D_s$ , and  $W_2$  are located in different layers of the medium. The background medium is identical to the previous simulation. The control regions  $W_1$  and  $W_2$  are defined in the spherical coordinates as

$$W_1 = \left\{ (r, \theta, \phi) : r \in [0.5, 0.55], \theta \in \left[ -\frac{\pi}{8}, \frac{\pi}{8} \right], \right. \\ \left. \phi \in \left[ \frac{3\pi}{4}, \frac{5\pi}{4} \right] \right\} + [0.1, 0, 0], \quad (27)$$

and

$$W_2 = \left\{ (r, \theta, \phi) : r \in [0.35, 0.4], \theta \in \left[ \frac{7\pi}{8}, \frac{9\pi}{8} \right], \right. \\ \left. \phi \in \left[ \frac{3\pi}{4}, \frac{5\pi}{4} \right] \right\} - [0.4, \pi, 0]. \quad (28)$$

In  $W_1$ , the prescribed radiating field is a plane EM wave propagating in the  $\hat{\mathbf{z}}$  direction. The electric field is polarized in the  $\hat{\mathbf{x}}$  direction, i.e. only  $\mathbf{E}_x$  is non-zero. As a result, the magnetic field only has the  $\mathbf{H}_y$  component. The prescribed field in  $W_2$  is null. The number of DoFs is the same as that in Subsection 5.1, i.e. 4212. However, the number of mesh points on the control regions is larger (set at 3960) than the one-region regime since more points are required to increase the control resolution. This is also due to the challenge posed by the contrast between the prescribed fields on the two neighboring control regions.

The simulation results are shown in Figure 6 for the “integral equation-TSVD” method and Figure 7 for the “integral equation-Tikhonov” method. In each figure, the first two rows respectively denote  $\mathbf{E}$  and  $\mathbf{H}$  in  $W_1$ , the third row is the absolute  $\mathbf{E}$  and  $\mathbf{H}$  in  $W_1$ . In particular, the three columns in the first two rows are the prescribed field, generated field, and the pointwise relative error, respectively. We observe that the generated  $\mathbf{E}$  and  $\mathbf{H}$  fields are in good agreement with the prescribed fields in both Figures 6 and 7. The maximum pointwise relative errors are less than 5%. The overall  $L^2$ -norm errors are within  $10^{-3}$ , especially, it is in order of  $10^{-4}$  for  $\mathbf{E}_x$  in Figure 6.

Very good control performance can likewise be observed in  $W_2$ . In the third row of Figure 6, the generated  $\mathbf{E}$  field is of order  $10^{-3}$  and the  $\mathbf{H}$  field is of order  $10^{-6}$ . Compared with the generated  $\mathbf{E}$  field in  $W_1$ , the magnitude of the field in  $W_2$  is almost three orders lower. A similar trend holds for the  $\mathbf{H}$  field. In particular, the radiated power in

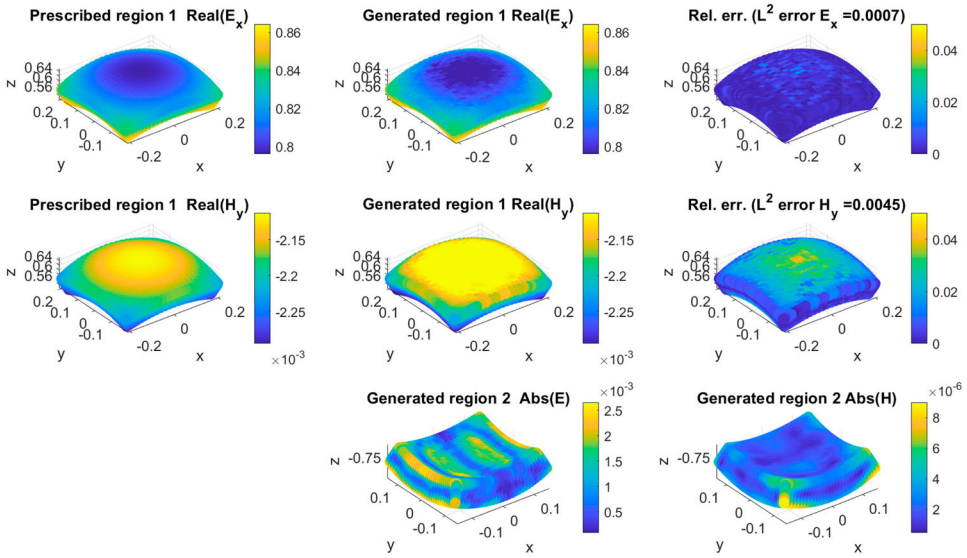


**Figure 6.** Electric and magnetic field synthesis in two exterior control regions by the “integral equation-TSVD” method.

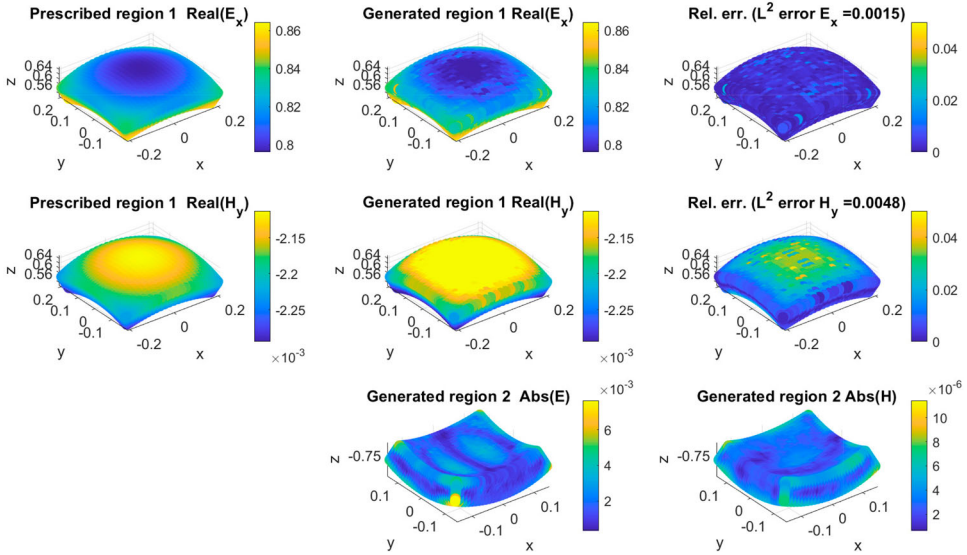


**Figure 7.** Electric and magnetic field synthesis in two exterior control regions by “integral equation-Tikhonov” method.

$W_2$  is about 60 dB lower than that in  $W_1$ . As such, one can conclude that a sharp EM contrast control is realized. The power is projected in  $W_1$  while the radiated power in  $W_2$  is suppressed.

The characterized currents are shown in Figure 8. The first subplot is the one obtained from the “integral equation-TSVD” method, while the second one shows the results of the “integral equation-Tikhonov” method. We find the magnitudes of both currents to be

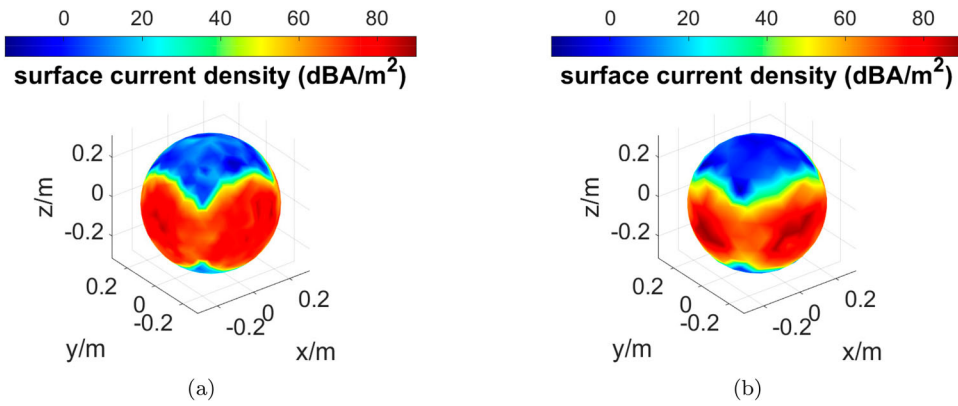


**Figure 8.** Characterized surface electric current ( $\mathbf{J}$ ) on the source  $\partial D_3$  to control EM fields in two regions. (a) “integral equation-TSVD” method. (b) “integral equation-Tikhonov” method.

quite large, indicating the need for high-powered sources. Unlike the one-region regime, the current distributions are very similar to the proposed methods. This observation can back up the statement that the Tikhonov regularized solution is essentially the same as the TSVD solution as long as the regularization parameter  $\alpha$  is sufficiently small.

**Remark 5.2:** In Subsection 5.2, we showed the contrast control where a plane wave is approximated in one region while the null field is realized in the other one. In theory, more control regions could be added so that the radiated field is forced to approximate more and more different patterns in multiple regions. This is far from a usual inverse source problem where one measures field data in the control regions that belongs to only one EM field interacting with the measurement apparatus.

### 6. Conclusion

This article presents a unified framework for actively manipulating electromagnetic fields in layered media. We cast the EM field manipulation problem as a linear inverse problem where the main goal is to characterize the current source from a complete knowledge of the desired field radiated outside the source region. Firstly, we formulated the model for the EM fields as a function of the current source using the integral equation method. We imposed the dyadic Green’s function in layered media on the integral equations to account for multiple reflections in the background medium. The source region and the control regions are suitably discretized. Thus, the integral equation is reduced to a discrete linear system by the method of moments. The resulting linear system is solved using some regularization methods to stabilize the solution, namely the truncated singular value decomposition (TSVD) method and the Tikhonov regularization method. An algorithm applying each of these regularization methods was developed.

We provided two simulations to illustrate the proposed algorithm and support our analyzes. The first experiment contains one control region and one source region. The second has two control regions and one source. In both simulations, we place the control region(s) and the source in the planar stratified medium. The simulation results demonstrate the existence of a current source (modeled as surface electric current) that can approximate

*a priori* given fields in some near control regions. In addition, we compared the control performance between the two approaches. In the one-region scenario, the “integral equation-TSVD” method outperforms the other method in control accuracy. However, the characterized current source by the “integral equation-TSVD” method requires higher power than the “integral equation-Tikhonov” approach. The high-power requirement could be a major limitation when the source is physically instantiated. The second simulation illustrated our methods’ capability of achieving the EM contrast control. In the first control region a plane wave was prescribed, while a null field was imposed on a nearby second control region. This contrast control scenario can be applied to focusing applications such as wireless power transfer, beamforming, etc. Overall, we observed that the calculated current sources can produce the EM fields with very small misfits between the generated and prescribed EM fields in control regions. Moreover, the current sources from the two approaches have a very similar distribution. The Tikhonov regularized solution is essentially the same as the TSVD solution as long as the regularization parameter  $\alpha$  is sufficiently small.

The results presented in this article strongly suggest the fact that in theory, we can characterize continuous current sources so that their radiated fields will approximate desired patterns in multiple mutually disjoint regions of space. This theoretical investigation will be the subject of our next research project.

## Disclosure statement

No potential conflict of interest was reported by the author(s).

## Funding

J. Chen and C. Qi would like to acknowledge the National Science Foundation, USA for funding their work under the award 1801925. D. Onofrei and N. J. A. Egarguin would like to acknowledge the Army Research Office, USA, for funding their work under the award W911NF-17-1-0478.

## References

- [1] Quijano JLA, Vecchi G. Field and source equivalence in source reconstruction on 3d surfaces. *Prog Electromagn Res*. 2010;103:67–100. doi: [10.2528/PIER10030309](https://doi.org/10.2528/PIER10030309)
- [2] Mohajer M, Safavi-Naeini S, Chaudhuri SK. Surface current source reconstruction for given radiated electromagnetic fields. *IEEE Trans Antennas Propag*. 2009;58(2):432–439. doi: [10.1109/TAP.2009.2037696](https://doi.org/10.1109/TAP.2009.2037696)
- [3] Kord A, Sounas DL, Alù A. Active microwave cloaking using parity-time-symmetric satellites. *Phys Rev Appl*. 2018;10(5):Article ID 054040. doi: [10.1103/PhysRevApplied.10.054040](https://doi.org/10.1103/PhysRevApplied.10.054040)
- [4] Chen A, Monticone F. Active scattering-cancellation cloaking: broadband invisibility and stability constraints. *IEEE Trans Antennas Propag*. 2019;68(3):1655–1664. doi: [10.1109/TAP.8](https://doi.org/10.1109/TAP.8)
- [5] Selvanayagam M, Eleftheriades GV. An active electromagnetic cloak using the equivalence principle. *IEEE Antennas Wirel Propag Lett*. 2012;11:1226–1229. doi: [10.1109/LAWP.2012.2224840](https://doi.org/10.1109/LAWP.2012.2224840)
- [6] Bisht MS, Srivastava KV. Controlling electromagnetic scattering of a cylindrical obstacle using concentric array of current sources. *IEEE Trans Antennas Propag*. 2020;68(12):8044–8052. doi: [10.1109/TAP.8](https://doi.org/10.1109/TAP.8)
- [7] Qian C, Zheng B, Shen Y, et al. Deep-learning-enabled self-adaptive microwave cloak without human intervention. *Nat Photonics*. 2020;14(6):383–390. doi: [10.1038/s41566-020-0604-2](https://doi.org/10.1038/s41566-020-0604-2)

- [8] Chen PY, Soric J, Alù A. Invisibility and cloaking based on scattering cancellation. *Adv Mater.* **2012**;24(44):OP281–OP304.
- [9] Selvanayagam M, Eleftheriades GV. Experimental demonstration of active electromagnetic cloaking. *Phys Rev X.* **2013**;3(4):Article ID 041011.
- [10] Sengupta S, Council H, Jackson DR, et al. Active radar cross section reduction of an object using microstrip antennas. *Radio Sci.* **2020**;55(2):1–20. doi: [10.1029/2019RS006939](https://doi.org/10.1029/2019RS006939)
- [11] Ang P, Eleftheriades GV. Active cloaking of a non-uniform scatterer. *Sci Rep.* **2020**;10(1):1–11. doi: [10.1038/s41598-019-56847-4](https://doi.org/10.1038/s41598-019-56847-4)
- [12] Lopéz YA, Andrés FLH, Pino MR, et al. An improved super-resolution source reconstruction method. *IEEE Trans Instrum Meas.* **2009**;58(11):3855–3866. doi: [10.1109/TIM.2009.2020847](https://doi.org/10.1109/TIM.2009.2020847)
- [13] Quijano JLA, Vecchi G. Improved-accuracy source reconstruction on arbitrary 3-d surfaces. *IEEE Antennas Wirel Propag Lett.* **2009**;8:1046–1049. doi: [10.1109/LAWP.2009.2031988](https://doi.org/10.1109/LAWP.2009.2031988)
- [14] Yao HM, Sha WE, Jiang LJ. Applying convolutional neural networks for the source reconstruction. *Prog Electromagn Res M.* **2018**;76:91–99. doi: [10.2528/PIERM18082907](https://doi.org/10.2528/PIERM18082907)
- [15] Foged L, Scialacqua L, Saccardi F, et al. Application of the dual-equation equivalent-current reconstruction to electrically large structures by fast multipole method enhancement [AMTA corner]. *IEEE Antennas Propag Mag.* **2014**;56(5):264–273. doi: [10.1109/MAP.74](https://doi.org/10.1109/MAP.74)
- [16] Persson K, Gustafsson M, Kristensson G, et al. Radome diagnostics – source reconstruction of phase objects with an equivalent currents approach. *IEEE Trans Antennas Propag.* **2014**;62(4):2041–2051. doi: [10.1109/TAP.2014.2298534](https://doi.org/10.1109/TAP.2014.2298534)
- [17] Álvarez Y, Las-Heras F, Pino MR. Reconstruction of equivalent currents distribution over arbitrary three-dimensional surfaces based on integral equation algorithms. *IEEE Trans Antennas Propag.* **2007**;55(12):3460–3468. doi: [10.1109/TAP.2007.910316](https://doi.org/10.1109/TAP.2007.910316)
- [18] Cai X, Geyi W. An optimization method for the synthesis of flat-top radiation patterns in the near-and far-field regions. *IEEE Trans Antennas Propag.* **2018**;67(2):980–987. doi: [10.1109/TAP.2018.2882653](https://doi.org/10.1109/TAP.2018.2882653)
- [19] Yu S, Liu H, Li L. Design of near-field focused metasurface for high-efficient wireless power transfer with multifocus characteristics. *IEEE Trans Ind Electron.* **2018**;66(5):3993–4002. doi: [10.1109/TIE.2018.2815991](https://doi.org/10.1109/TIE.2018.2815991)
- [20] Ayestarán RG. Fast near-field multifocusing of antenna arrays including element coupling using neural networks. *IEEE Antennas Wirel Propag Lett.* **2018**;17(7):1233–1237. doi: [10.1109/LAWP.2018.2840540](https://doi.org/10.1109/LAWP.2018.2840540)
- [21] Iliopoulos I, Fuchs B, Sauleau R, et al. On the use of convex optimization for electromagnetic near-field shaping. In: *2017 11th European Conference on Antennas and Propagation (EUCAP)*. IEEE; 2017. p. 1013–1016
- [22] Ayestarán RG, León G, Pino MR, et al. Wireless power transfer through simultaneous near-field focusing and far-field synthesis. *IEEE Trans Antennas Propag.* **2019**;67(8):5623–5633. doi: [10.1109/TAP.8](https://doi.org/10.1109/TAP.8)
- [23] Nepa P, Buffi A. Near-field-focused microwave antennas: near-field shaping and implementation. *IEEE Antennas Propag Mag.* **2017**;59(3):42–53. doi: [10.1109/MAP.2017.2686118](https://doi.org/10.1109/MAP.2017.2686118)
- [24] Iliopoulos I, Fuchs B, Sauleau R, et al. Scalar near-field focusing in lossy media. In: *2017 International Conference on Electromagnetics in Advanced Applications (ICEAA)*. IEEE; 2017. p. 718–721
- [25] Wu JW, Wu RY, Bo XC, et al. Synthesis algorithm for near-field power pattern control and its experimental verification via metasurfaces. *IEEE Trans Antennas Propag.* **2018**;67(2):1073–1083. doi: [10.1109/TAP.2018.2882645](https://doi.org/10.1109/TAP.2018.2882645)
- [26] Clauzier S, Mikki SM, Antar YM. Design of near-field synthesis arrays through global optimization. *IEEE Trans Antennas Propag.* **2014**;63(1):151–165. doi: [10.1109/TAP.2014.2367536](https://doi.org/10.1109/TAP.2014.2367536)
- [27] Egarguin NJA, Jackson DR, Onofrei D, et al. Adaptive beamforming using scattering from a drone swarm. In: *2020 IEEE Texas symposium on wireless and microwave circuits and systems (WMCS)*. Waco (TX): IEEE; 2020. p. 1–6.
- [28] Brown T, Narendra C, Vahabzadeh Y, et al. On the use of electromagnetic inversion for metasurface design. *IEEE Trans Antennas Propag.* **2019**;68(3):1812–1824. doi: [10.1109/TAP.8](https://doi.org/10.1109/TAP.8)

- [29] Huang C, Zhang C, Yang J, et al. Reconfigurable metasurface for multifunctional control of electromagnetic waves. *Adv Opt Mater.* 2017;5(22):Article ID 1700485. doi: [10.1002/adom.v5.22](https://doi.org/10.1002/adom.v5.22)
- [30] Boardman A, Alberucci A, Assanto G, et al. Waves in hyperbolic and double negative metamaterials including rogues and solitons. *Nanotechnology.* 2017;28(44):Article ID 444001. doi: [10.1088/1361-6528/aa6792](https://doi.org/10.1088/1361-6528/aa6792)
- [31] Kurilkina SN, Petrov NS, Zimin AB, et al. Special inhomogeneous electromagnetic waves in hyperbolic metamaterials. *J Opt.* 2017 Nov;19(12):Article ID 125102. doi: [10.1088/2040-8986/aa945c](https://doi.org/10.1088/2040-8986/aa945c)
- [32] Chen J, Hu S, Zhu S, et al. Metamaterials: from fundamental physics to intelligent design. *Interdiscip Materials.* 2022 Jul;2:8.
- [33] Yin X, Zhu H, Guo H, et al. Hyperbolic metamaterial devices for wavefront manipulation. *Laser Photon Rev.* 2018;13:2–4.
- [34] Desouky M, Mahmoud A, Swillam M. Tunable mid IR focusing in InAs based semiconductor hyperbolic metamaterial. *Sci Rep.* 2017;7:2–3. doi: [10.1038/s41598-017-15493-4](https://doi.org/10.1038/s41598-017-15493-4)
- [35] Lee S, Baek S, Kim T, et al. Metamaterials for enhanced optical responses and their application to active control of terahertz waves. *Adv Mater.* 2020;32(35):3–5.
- [36] Abdelraouf O, Wang Z, Liu H, et al. Recent advances in tunable metasurfaces: materials, design, and applications. *ACS Nano.* 2022;16(9):Article ID 13339. doi: [10.1021/acsnano.2c04628](https://doi.org/10.1021/acsnano.2c04628)
- [37] Marengo EA, Devaney AJ. The inverse source problem of electromagnetics: linear inversion formulation and minimum energy solution. *IEEE Trans Antennas Propag.* 1999;47(2):410–412. doi: [10.1109/8.761085](https://doi.org/10.1109/8.761085)
- [38] Egarguin NJA, Onofrei D, Qi C, et al. Active manipulation of Helmholtz scalar fields in an ocean of two homogeneous layers of constant depth. *Inverse Probl Sci Eng.* 2021;29(13):1–25.
- [39] Qi C, Egarguin NJA, Onofrei D, et al. Feasibility analysis for active near/far field acoustic pattern synthesis in free space and shallow water environments. *Acta Acust.* 2021;5:39. doi: [10.1051/aacus/2021030](https://doi.org/10.1051/aacus/2021030)
- [40] Egarguin NJA, Onofrei D, Qi C, et al. Active manipulation of Helmholtz scalar fields: near-field synthesis with directional far-field control. *Inverse Probl.* 2020;36(9):Article ID 095005. doi: [10.1088/1361-6420/aba106](https://doi.org/10.1088/1361-6420/aba106)
- [41] Onofrei D. Active manipulation of fields modeled by the Helmholtz equation. *J Integral Equ Appl.* 2014;26(4):553–572. doi: [10.1216/JIE-2014-26-4-553](https://doi.org/10.1216/JIE-2014-26-4-553)
- [42] Egarguin NJA, Onofrei D, Platt E. Sensitivity analysis for the active manipulation of Helmholtz fields in 3d. *Inverse Probl Sci Eng.* 2020;28(3):314–339. doi: [10.1080/17415977.2018.1555248](https://doi.org/10.1080/17415977.2018.1555248)
- [43] Onofrei D, Platt E. On the synthesis of acoustic sources with controllable near fields. *Wave Motion.* 2018;77:12–27. doi: [10.1016/j.wavemoti.2017.10.004](https://doi.org/10.1016/j.wavemoti.2017.10.004)
- [44] Zeng S, Egarguin NJA, Onofrei D, et al. Active control of electromagnetic waves in layered media using a current source. In: 2020 IEEE Texas symposium on wireless and microwave circuits and systems (WMCS). Waco (TX): IEEE; 2020. p. 1–6.
- [45] Onofrei D, Platt E, Egarguin NJA. Active manipulation of exterior electromagnetic fields by using surface sources. *Q Appl Math.* 2020;78(4):641–670. doi: [10.1090/qam/2020-78-04](https://doi.org/10.1090/qam/2020-78-04)
- [46] Merzlikin AM, Puzko RS. Homogenization of Maxwell's equations in a layered system beyond the static approximation. *Sci Rep.* 2020;10(1):Article ID 15783. doi: [10.1038/s41598-020-72727-8](https://doi.org/10.1038/s41598-020-72727-8)
- [47] Angell TS, Kirsch A. Optimization methods in electromagnetic radiation. Springer Science & Business Media; 2004.
- [48] Qi C, Egarguin NJA, Zeng S, et al. Sensitivity analysis for active electromagnetic field manipulation in free space. *Appl Math Sci.* 2022;30(1):661–687. doi: [10.1080/27690911.2022.2118270](https://doi.org/10.1080/27690911.2022.2118270)
- [49] Epstein CL, Greengard L. Debye sources and the numerical solution of the time harmonic Maxwell equations. *Commun Pure Appl Math.* 2010;63(4):413–463.
- [50] Xiong XYZ, Sha WEI, Jun Jiang L. Helmholtz decomposition based on integral equation method for electromagnetic analysis. *Microw Opt Technol Lett.* 2014;56(8):1838–1843. doi: [10.1002/mop.v56.8](https://doi.org/10.1002/mop.v56.8)
- [51] O'Neil M. A generalized Debye source approach to electromagnetic scattering in layered media. *J Math Phys.* 2014;55(1):Article ID 012901. doi: [10.1063/1.4862747](https://doi.org/10.1063/1.4862747)

- [52] Fu X, Li J, Jiang LJ, et al. Generalized Debye sources-based EFIE solver on subdivision surfaces. *IEEE Trans Antennas Propag.* 2017;65(10):5376–5386. doi: [10.1109/TAP.2017.2740976](https://doi.org/10.1109/TAP.2017.2740976)
- [53] Epstein CL, Rachh M. Debye source representations for type-I superconductors, I: the static type I case. *J Comput Phys.* 2022;452:Article ID 110892. doi: [10.1016/j.jcp.2021.110892](https://doi.org/10.1016/j.jcp.2021.110892)
- [54] Michalski KA, Mosig JR. Multilayered media Green's functions in integral equation formulations. *IEEE Trans Antennas Propag.* 1997;45(3):508–519. doi: [10.1109/8.558666](https://doi.org/10.1109/8.558666)
- [55] Li D, Wilton DR, Jackson DR, et al. Efficient computation of Green's functions for lossy uniaxial anisotropic layered media. *Radio Sci.* 2019;54(3):196–214. doi: [10.1029/2018RS006648](https://doi.org/10.1029/2018RS006648)
- [56] Aksun M, Dural G. Clarification of issues on the closed-form Green's functions in stratified media. *IEEE Trans Antennas Propag.* 2005;53(11):3644–3653. doi: [10.1109/TAP.2005.858571](https://doi.org/10.1109/TAP.2005.858571)
- [57] Li D, Wilton DR, Jackson DR. Recent advances in evaluating Green's functions for multilayered media and half-space problems. In: 2017 computing and electromagnetics international workshop (CEM). Barcelona (Spain): IEEE; 2017. p. 1–2.
- [58] Simsek E, Liu QH, Wei B. Singularity subtraction for evaluation of Green's functions for multilayer media. *IEEE Trans Microw Theory Tech.* 2006;54(1):216–225. doi: [10.1109/TMTT.2005.860304](https://doi.org/10.1109/TMTT.2005.860304)
- [59] Michalski KA. Extrapolation methods for Sommerfeld integral tails. *IEEE Trans Antennas Propag.* 1998;46(10):1405–1418. doi: [10.1109/8.725271](https://doi.org/10.1109/8.725271)
- [60] Mosig J. The weighted averages algorithm revisited. *IEEE Trans Antennas Propag.* 2012;60(4):2011–2018. doi: [10.1109/TAP.2012.2186244](https://doi.org/10.1109/TAP.2012.2186244)
- [61] Rao S, Wilton D, Glisson A. Electromagnetic scattering by surfaces of arbitrary shape. *IEEE Trans Antennas Propag.* 1982;30(3):409–418. doi: [10.1109/TAP.1982.1142818](https://doi.org/10.1109/TAP.1982.1142818)
- [62] Mueller JL, Siltanen S. Linear and nonlinear inverse problems with practical applications. SIAM; 2012.
- [63] Bonesky T. Morozov's discrepancy principle and Tikhonov-type functionals. *Inverse Probl.* 2008;25(1):Article ID 015015. doi: [10.1088/0266-5611/25/1/015015](https://doi.org/10.1088/0266-5611/25/1/015015)

## Appendix. Dyadic Green's function in spatial domain

Taking the inverse 2-D Fourier transform, the spectral-domain Green's function can be converted back to the spatial domain. In (11), the evaluation of  $\mathcal{G}^{EJ}$  involves double infinite integral, which can be computationally intensive when the number of observation points is large. To accelerate the computation of (11), the Hankel transform is applied to reduce the double infinite integral into a single semi-infinite integral. The general Hankel transform is written as

$$\begin{aligned} F(\boldsymbol{\rho} - \boldsymbol{\rho}', z, z') &= \mathcal{S}_n\{\tilde{F}(k_\rho, z, z')\} \\ &= \frac{1}{2\pi} \int_0^\infty \tilde{F}(\mathbf{k}_\rho, z, z') J_n(k_\rho |\boldsymbol{\rho} - \boldsymbol{\rho}'|) k_\rho dk_\rho, \end{aligned} \quad (\text{A1})$$

where the integral operator  $\mathcal{S}_n\{\cdot\}$  is called the generalized Sommerfeld integral (SI).  $J_n$  is the Bessel function of the first kind of order  $n$  with  $n = 0, 1, 2$ .  $\boldsymbol{\rho}$  and  $\boldsymbol{\rho}'$  respectively denote the transverse projection of the observation point  $\mathbf{r}$  and source point  $\mathbf{r}'$  in  $xy$ -plane.

Therefore, the dyadic Green's function can be expressed with respect to 16 SIs,

$$\begin{aligned} \mathcal{G}^{EJ}(\boldsymbol{\rho} - \boldsymbol{\rho}', z, z') &= \begin{bmatrix} \frac{-I_1 + \cos(2\gamma)I_{13}}{2} & \frac{\sin(2\gamma)I_{13}}{2} & \frac{\cos(\gamma)I_7}{j\omega\varepsilon_0\varepsilon'_z} \\ \frac{\sin(2\gamma)I_{13}}{2} & \frac{-I_1 - \cos(2\gamma)I_{13}}{2} & \frac{\sin(\gamma)I_7}{j\omega\varepsilon_0\varepsilon'_z} \\ \frac{\cos(\gamma)I_{12}}{j\omega\varepsilon_0\varepsilon_z} & \frac{\sin(\gamma)I_{12}}{j\omega\varepsilon_0\varepsilon_z} & \frac{I_5}{j\omega\varepsilon_0\varepsilon_z} - \delta(\mathbf{r}' - \mathbf{r}) \end{bmatrix} \end{aligned} \quad (\text{A2})$$

$$\mathcal{G}^{EM}(\boldsymbol{\rho} - \boldsymbol{\rho}', z, z')$$

$$= \begin{bmatrix} \frac{-\sin(2\gamma)I_{15}}{2} & \frac{-I_3 + \cos(2\gamma)I_{15}}{2} & \frac{\sin(\gamma)I_9}{j\omega\mu_0\mu'_z} \\ \frac{I_3 + \cos(2\gamma)I_{15}}{2} & \frac{\sin(2\gamma)I_{15}}{2} & \frac{\cos(\gamma)I_9}{j\omega\mu_0\mu'_z} \\ \frac{-\sin(\gamma)I_{10}}{j\omega\varepsilon_0\varepsilon_z} & \frac{\cos(\gamma)I_{10}}{j\omega\varepsilon_0\varepsilon_z} & 0 \end{bmatrix} \quad (\text{A3})$$

$$\mathcal{G}^{HJ}(\boldsymbol{\rho} - \boldsymbol{\rho}', z, z')$$

$$= \begin{bmatrix} \frac{\sin(2\gamma)I_{16}}{2} & \frac{I_4 - \cos(2\gamma)I_{16}}{2} & \frac{-\sin(\gamma)I_{10}}{j\omega\varepsilon_0\varepsilon'_z} \\ \frac{-I_4 - \cos(2\gamma)I_{16}}{2} & \frac{-\sin(2\gamma)I_{16}}{2} & \frac{\cos(\gamma)I_{10}}{j\omega\varepsilon_0\varepsilon'_z} \\ \frac{\sin(\gamma)I_9}{j\omega\mu_0\mu_z} & \frac{-\cos(\gamma)I_9}{j\omega\mu_0\mu_z} & 0 \end{bmatrix} \quad (\text{A4})$$

$$\mathcal{G}^{HM}(\boldsymbol{\rho} - \boldsymbol{\rho}', z, z')$$

$$= \begin{bmatrix} \frac{-I_2 + \cos(2\gamma)I_{14}}{2} & \frac{\sin(2\gamma)I_{14}}{2} & \frac{\cos(\gamma)I_8}{j\omega\mu_0\mu'_z} \\ \frac{\sin(2\gamma)I_{14}}{2} & \frac{-I_2 - \cos(2\gamma)I_{14}}{2} & \frac{\sin(\gamma)I_8}{j\omega\mu_0\mu'_z} \\ \frac{\cos(\gamma)I_{11}}{j\omega\mu_0\mu_z} & \frac{\sin(\gamma)I_{11}}{j\omega\mu_0\mu_z} & \frac{I_6}{j\omega\mu_0\mu_z} - \delta(\mathbf{r}' - \mathbf{r}) \end{bmatrix} \quad (\text{A5})$$

where cosine and sine functions in (A2)–(A5) are defined as

$$\begin{aligned} \cos(\gamma) &= \frac{x - x'}{|\boldsymbol{\rho} - \boldsymbol{\rho}'|} \\ \sin(\gamma) &= \frac{y - y'}{|\boldsymbol{\rho} - \boldsymbol{\rho}'|} \\ \cos(2\gamma) &= \frac{(x - x')^2 - (y - y')^2}{|\boldsymbol{\rho} - \boldsymbol{\rho}'|^2} \\ \sin(2\gamma) &= 2 \frac{(x - x')(y - y')}{|\boldsymbol{\rho} - \boldsymbol{\rho}'|^2} \end{aligned} \quad (\text{A6})$$

$I_i, i = 1, 2, \dots, 16$  denote 16 independent SIs. The discussion of the SIs is beyond the scope of this article. More details can be referred to [55].